Relativistic ionization characteristics of laser-driven hydrogenlike ions

Heiko Bauke,[*] Henrik G. Hetzheim,[†] Guido R. Mocken, Matthias Ruf, and Christoph H. Keitel[‡]
Max-Planck-Institut für Kernphysik, Saupfercheckweg 1, 69117 Heidelberg, Germany
(Received 21 March 2011; published 20 June 2011)

In this contribution, we investigate the relativistic ionization characteristics of highly charged hydrogenlike ions in short intense laser pulses as a function of the laser pulse parameters by means of the numerical solution of the time-dependent Dirac equation and the time-dependent Klein-Gordon equation as well as by the classical phase-space averaging method. For this purpose, we generalize the phase-space averaging method such that it is applicable to relativistically driven particles in arbitrary central potentials. If the ionization probability is not too small, quantum mechanical and classical methods give similar results for laser wavelengths in the range from the near-infrared to soft x-ray radiation. We find that ionization in few-cycle intense laser pulses depends sensitively on the pulses' peak intensity but little on the pulse tails and on the pulse energy. The ionization probability is shown to be strongly linked to the peak intensity allowing for an estimation of the laser intensity via ionization yields.

DOI: 10.1103/PhysRevA.83.063414 PACS number(s): 32.80.Rm, 31.30.J−, 42.65.−k, 41.75.Jv

I. INTRODUCTION

Current high-power petawatt lasers reach intensities of the order of $10^{22}\,\mathrm{W/cm^2}$ [1]. The mean field strength for these lasers is several orders of magnitude higher than the Coulomb field strength in a hydrogen atom at the distance of a Bohr radius from the nucleus. Lasers with high intensities in the relativistic optical regime have been employed to investigate strong laser-matter interactions, e.g., to study nuclear interactions [2], relativistic quantum optics [3], and γ-ray emission [4] or to test the validity of quantum electrodynamics through vacuum polarization [5]. High-intensity lasers also have applications in cancer therapy [6].

Apart from the increase of the maximum intensity, progress in laser technology allows to push the laser wavelength from the optical to the x-ray range, e.g., by x-ray free electron lasers (XFELs) [7]. Thus, a new wavelength regime of strong-field laser-matter interaction is available reaching from the ultraviolet to the x-ray regime. Furthermore, it is experimentally possible to control these intense lasers to form attosecond pulses [8]. Measurements of the carrier envelope phase of pulses in the infrared and the ultraviolet have been demonstrated in [9].

However, the accurate determination of high-intensity laser parameters, particularly the intensity in the relativistic regime, is still challenging. A laser's intensity may be inferred from photoionization of atoms or clusters [10]. The generation of highly charged ions is nowadays possible for essentially every charge state. Sending atoms through thin foils allows to generate ions with high purity and high density [11]. Thus, in [12] it is proposed to determine the intensity of very high intensity lasers sensitively by measuring the ionization probability [13] of multiply charged hydrogenlike ions. Because the above-the-threshold-intensity grows proportionately to the sixth power of the atomic number, determining the laser intensity by measuring the ionization probability may be implemented for a wide range of intensities from about $10^{14}\,\mathrm{W/cm^2}$ to about $10^{26}\,\mathrm{W/cm^2}$ using different kinds of hydrogenlike ions. However, this requires knowing the relation between ionization probability, intensity, wavelength, and pulse shape. The ionization of atomic, molecular, and cluster targets [13–15] in intense laser fields has been investigated by several experiments. The numerical solution of the time-dependent Schrödinger equation allows the study of the ionization of hydrogen and hydrogenlike ions for various laser frequencies and a large variety of pulse lengths and intensities theoretically [15,16].

For atomic numbers larger than $Z = 14$, the velocity of the (classical) electron in a hydrogenlike ion exceeds 10% of the speed of light. Thus, for hydrogenlike ions with atomic numbers larger than $Z = 14$, we enter the weakly relativistic regime. Relativistic effects may also be induced by a strong external electromagnetic field if the laser field parameter [17] ξ is of the order of one or larger. Thus, the ionization dynamics of highly charged hydrogenlike ions necessitates a relativistic treatment [15].

Ionization in the weakly relativistic regime may be studied, e.g., by the numerical solution of the weakly relativistic Schrödinger equation [18]. For highly relativistic electrons, however, one has to solve the time-dependent Dirac equation [19] or the Klein-Gordon equation [20], provided that the spin of the electron can be neglected. A numerical solution of the Dirac or Klein-Gordon equation is computationally expensive because a huge excursion amplitude of the electron leaving the ionic core needs to be resolved in real space as well as in momentum space requiring large grids with high resolution. Furthermore, the solution of the time-dependent Dirac or Klein-Gordon equation requires much smaller time steps as compared to the time-dependent Schrödinger equation due to the relativistic rest mass energy. Classical trajectory Monte Carlo simulations [21] offer an alternative approach to study the ionization process of hydrogenlike ions in laser fields. This method is less computationally expensive than the solution of quantum wave equations but it neglects genuine quantum effects.

[*]bauke@mpi-hd.mpg.de
[†]Current affiliation: Deutsches Krebsforschungszentrum, Im Neuenheimer Feld 280, 69120 Heidelberg, Germany.
[‡]keitel@mpi-hd.mpg.de

In this contribution, we study the ionization of highly charged hydrogenlike ions by few-cycle intense laser pulses by solving the time-dependent Dirac equation and the time-dependent Klein-Gordon equation numerically as well as by classical Monte Carlo methods. We investigate how ionization probabilities depend on laser parameters and the pulse form focusing on laser pulses in the XFEL regime. Because of computational limitations we restrict our quantum mechanical simulations to one and two dimensions. To be able to compare one- and two-dimensional quantum calculations with soft-core potentials and classical Monte Carlo methods we generalize the relativistic phase-space averaging method for the Coulomb potential [22] to general central potentials in one, two, and, three dimensions.

This paper is organized as follows. In Sec. II, we provide an overview of the computational techniques utilized in our investigations, and a comparison of the two different numerical approaches follows in Sec. III. The electron dynamics in ultrastrong laser fields and the ionization probability are studied in Sec. IV. In Sec. V we compare our findings, as obtained by the solution of the time-dependent Dirac equation and the relativistic phase-space averaging method, with results that may be obtained by the application of the WKB method. Finally, our results are summarized in Sec. VI.

II. PHYSICAL SETUPS AND COMPUTATIONAL TECHNIQUES

In order to study ionization dynamics in ultrastrong laser fields in various laser setups we apply different computational techniques: the numerical propagation of Dirac wave functions and Klein-Gordon wave functions, and the relativistic phase-space averaging method.

A. Physical setups

In all our numerical simulations we consider initially bound electrons of rest mass m and charge $-e$ evolving in an attractive central potential and in a strong external electromagnetic field of a linearly polarized laser pulse traveling at the speed of light c, having the wavelength λ, the angular frequency $\omega = 2\pi c/\lambda$, and the wave number $k = \omega/c$. Introducing the phase

$$\eta = k\boldsymbol{n}\cdot\boldsymbol{x} - \omega t, \tag{1}$$

the laser's electromagnetic fields $\boldsymbol{E}_L(\boldsymbol{x},t)$ and $\boldsymbol{B}_L(\boldsymbol{x},t)$ are given as functions of position $\boldsymbol{x}$ and time t by

$$\boldsymbol{E}_L(\boldsymbol{x},t) = \boldsymbol{E}_{L,\max} w(\eta,j)\sin(\eta+\alpha_L), \tag{2a}$$

$$\boldsymbol{B}_L(\boldsymbol{x},t) = \frac{1}{c}\boldsymbol{n}\times\boldsymbol{E}_{L,\max} w(\eta,j)\sin(\eta+\alpha_L). \tag{2b}$$

In (1) and (2) $w(\eta,j)$ is an envelope function and $\boldsymbol{n} = (1,0,0)^T$ denotes the propagation direction; $\boldsymbol{E}_{L,\max} = (0,E_{L,\max},0)^T$ is the maximal electric field strength vector, and α_L allows for a possible phase shift. For one-dimensional systems the magnetic field component has to vanish and the electric component reduces to $E_L(x,t) = E_{L,\max} w(-\omega t,j)\sin(\alpha_L - \omega t)$.

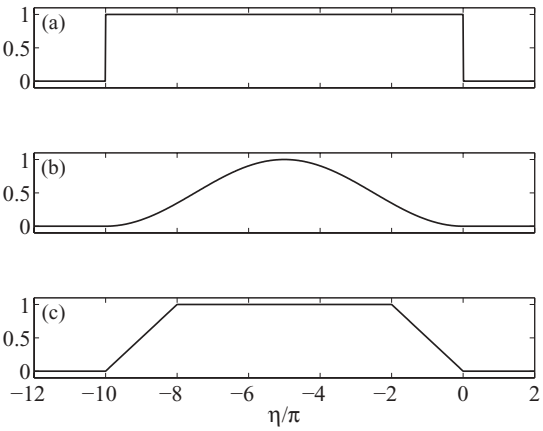

FIG. 1. Illustration of the employed envelope functions (3), from top to bottom $w_{\text{rect}}(\eta,10)$, $w_{\sin^2}(\eta,10)$, and $w_{\text{ramp}}(\eta,10,2)$.

The envelope function $w(\eta,j)$ forms the pulse shape. We will apply rectangular windows

$$w_{\text{rect}}(\eta,j) = \begin{cases} 1 & \text{if} \quad -j\pi \leqslant \eta \leqslant 0, \\ 0 & \text{otherwise}, \end{cases} \tag{3a}$$

($\sin^2$) envelopes

$$w_{\sin^2}(\eta,j) = \begin{cases} \sin^2(\pi+\eta/j) & \text{if} \quad -j\pi \leqslant \eta \leqslant 0, \\ 0 & \text{otherwise}, \end{cases} \tag{3b}$$

as well as envelopes with linear on-off-ramps

$$w_{\text{ramp}}(\eta,j,l) = \begin{cases} (\eta+j\pi)/(l\pi) & \text{if} \quad -j \leqslant \eta/\pi \leqslant -j+l, \\ 1 & \text{if} \quad -j+l \leqslant \eta/\pi \leqslant -l, \\ -\eta/(l\pi) & \text{if} \quad -l \leqslant \eta/\pi \leqslant 0, \\ 0 & \text{otherwise}. \end{cases} \tag{3c}$$

Each laser pulse has a spatial extent of $j\lambda/2$ in the propagation direction but is of infinite width perpendicular to the propagation direction. The on-off-ramps of $w_{\text{ramp}}(\eta,j,l)$ have lengths of $l\lambda/2$. See Fig. 1 for some illustrative examples of the employed envelope functions (3).

The attractive central potential is modeled by a Coulomb potential

$$V(|\boldsymbol{x}|) = -\frac{\alpha}{|\boldsymbol{x}|} \quad \text{with} \quad \alpha = \frac{e^2 Z}{4\pi\varepsilon_0}, \tag{4}$$

where Z denotes the atomic number and ε_0 the electric permittivity of the vacuum. The electron dynamics during the ionization process is mainly governed by an oscillation in the laser polarization direction and an additional drift in the laser propagation direction caused by the Lorentz force. Thus, it is sufficient to describe the ionization dynamics in the two-dimensional plane of the laser's polarization direction and its propagation direction to cover the essential features of the electron dynamics. While restricting the electron wave dynamics to two dimensions, the singularity of the Coulomb potential is overemphasized. Therefore, we replace the Coulomb potential by a soft-core potential

$$V(|\boldsymbol{x}|) = -\frac{\alpha}{\sqrt{|\boldsymbol{x}|^2+\zeta^2}} \tag{5}$$

for lower dimensional settings. The soft-core parameter ζ models the missing third dimension and avoids the singularity of the Coulomb potential.

B. Propagation of relativistic quantum wave functions

Solving the time-dependent Dirac equation or the Klein-Gordon equation allows us to study the ionization in ultrastrong laser fields including all quantum features. The evolution of the four-component Dirac spinor wave function $\Psi(\boldsymbol{x},t)$ is determined by

$$i\hbar\frac{\partial\Psi(\boldsymbol{x},t)}{\partial t} = \left[c\boldsymbol{\alpha}\cdot\left(\frac{\hbar}{i}\nabla + e\boldsymbol{A}(\boldsymbol{x},t)\right) + V(|\boldsymbol{x}|) + \beta mc^2\right]\Psi(\boldsymbol{x},t), \tag{6}$$

with $\boldsymbol{\alpha} = (\alpha_1,\alpha_2,\alpha_3)$, β denoting the Dirac matrices. Neglecting the spin of the electron leads to the Klein-Gordon equation in the Feshbach-Villars representation [23]

$$i\hbar\frac{\partial\Psi(\boldsymbol{x},t)}{\partial t} = \left[\frac{\tau_3 + i\tau_2}{2m}\left(\frac{\hbar}{i}\nabla + e\boldsymbol{A}(\boldsymbol{x},t)\right)^2 + V(|\boldsymbol{x}|) + \tau_3 mc^2\right]\Psi(\boldsymbol{x},t), \tag{7}$$

where $\Psi(\boldsymbol{x},t)$ is a two component wave function and τ_i denote the Pauli matrices. The vector potential $\boldsymbol{A}(\boldsymbol{x},t)$ in (6) and (7) specifies the electromagnetic laser fields, viz., $\boldsymbol{E}_L(\boldsymbol{x},t) = -\partial\boldsymbol{A}(\boldsymbol{x},t)/\partial t$ and $\boldsymbol{B}_L(\boldsymbol{x},t) = \nabla\times\boldsymbol{A}(\boldsymbol{x},t)$.

The ionization dynamics of the electron is obtained by solving the time-dependent equations (6) and (7) numerically. For the Dirac equation (6) we utilize the Fourier split-operator method [19,24,25], which is more accurate than approaches based on finite-difference schemes [26]. The basic idea of the Fourier split-operator method is to replace the time evolution operator that is generated by the Dirac Hamiltonian in (6) by a product of operators that are diagonal either in real space or in momentum space and to propagate the wave function alternately in real space and momentum space. The two-component representation (7) of the Klein-Gordon equation allows us to propagate the Klein-Gordon equation entirely in real space [20] by a split operator scheme. In contrast to the Fourier split operator method for the Dirac equation, we can avoid the Fourier transformations in each propagation step. Thus, the algorithm may be efficiently parallelized on parallel computers by a domain decomposition. This leads to an enormous reduction of computation time and enables us to consider laser pulses with larger wavelength than it is possible for the Dirac equation. In order to reduce computing time, we solve the time-dependent Dirac equation and the Klein-Gordon equation for only one- and two-dimensional systems. Furthermore, the employed numerical schemes propagate the wave function on an adaptive grid that may grow or shrink according to the wave function dynamics.

The initial quantum state is the ground state of the potential $V(\boldsymbol{x})$ which may be obtained by a spectral method introduced by Feit *et al.* [19,24]. After the laser pulse has passed the hydrogenlike ion, we propagate the wave packet further to some final time t_{end} to determine the ionization probability p_{ion}. It may be calculated by projecting the wave function $\Psi(\boldsymbol{x},t_{\text{end}})$ onto the bound field-free eigenstates $\Psi_i(\boldsymbol{x})$

$$p_{\text{ion}} = 1 - \sum_i \left|\int \Psi_i(\boldsymbol{x})^*\Psi(\boldsymbol{x},t_{\text{end}})\,d^2x\right|^2. \tag{8}$$

However, it is challenging to determine *all* bound eigenstates $\Psi_i(\boldsymbol{x})$ because the soft-core-potential's non-ground-state eigenstates are degenerated and energy level spacings become narrow near the continuum energy band. Thus, Eq. (8) is not a practicable method and we use an alternative approach. We calculate the ionization fraction by comparing the spatial distribution of the electron density $|\Psi(\boldsymbol{x},t)|^2$ before and after the interaction of the electron with the laser field. Before the interaction with the laser field, we choose a quadratic area (indicated by $\square$) around the center of the soft-core potential that is as small as possible but large enough to carry all relevant parts of a (normalized) bound state, viz.,

$$\int_{\square}\Psi(\boldsymbol{x},0)^*\Psi(\boldsymbol{x},0)\,d^2x \approx 1. \tag{9}$$

After the interaction with the laser field the ionization probability is given by an integral of the electron density over the quadratic area,

$$p_{\text{ion}} = 1 - \int_{\square}\Psi(\boldsymbol{x},t_{\text{end}})^*\Psi(\boldsymbol{x},t_{\text{end}})\,d^2x. \tag{10}$$

Note that the time t_{end} has to be large enough to ensure that the ionized part and the bound part of the wave packet are well separated and the computational grid has to be much larger than the quadratic area in (9) and (10).

The solution of the time-dependent Dirac or Klein-Gordon equation comprises all quantum mechanical characteristics of the ionization process. However, the relativistic total energy of the electron of the order mc^2 limits the maximal temporal step size that can be taken in each step of the split-operator method to $\Delta t \ll \hbar/(mc^2)$. This renders the numerical propagation of relativistic wave functions into a computationally expensive task. In order to study the ionization dynamics of hydrogenlike ions in laser pulses having a length of about 7.25 nm, we have to propagate the wave function over about an atomic unit of time $\hbar/(mc^2\alpha_{\text{em}}^2) \approx 2\times10^{-17}$ s, with the fine-structure constant $\alpha_{\text{em}} \approx 1/137$, requiring more than $1/\alpha_{\text{em}}^2 \approx 2\times10^4$ time steps. Realistic laser pulses might be much longer requiring even more time steps.

Thus, in order to cope with computational and numerical limitations in solving the time-dependent Dirac or Klein-Gordon equation, we have to introduce two important approximations: We reduce the dimensionality to two dimensions and we replace the Coulomb potential by a soft-core potential (5). The replacement of the three-dimensional Coulomb potential by a two-dimensional soft-core potential prevents inferring *quantitative* results from the evolution of the wave function that could be directly compared with the outcome of an experiment. However, the solution of the two-dimensional Dirac equation or Klein-Gordon equation allows us to analyze the ionization process qualitatively.

C. Relativistic phase-space averaging method

The phase-space averaging method approximates a quantum dynamical process by replacing the motion of a wave function by an ensemble of classical single-particle trajectories $(\boldsymbol{x}(t),\boldsymbol{p}(t))$. Single-particle observables at time t are functions of the position $\boldsymbol{x}(t)$ and the momentum $\boldsymbol{p}(t)$. The quantum mechanical expectation value of an observable O at time t is replaced by

$$\langle O\rangle(t) = \int\int O(\boldsymbol{x}(t),\boldsymbol{p}(t))p(\boldsymbol{x}(t),\boldsymbol{p}(t))\,d^3x\,d^3p, \quad (11)$$

where $p(\boldsymbol{x}(t),\boldsymbol{p}(t))\,d^3x\,d^3p$ denotes the probability of finding a particle at time t in a phase-space volume $d^3x\,d^3p$ around $(\boldsymbol{x}(t),\boldsymbol{p}(t))$. In a numerical implementation of the phase-space averaging method, only a finite number N of single-particle trajectories $(\boldsymbol{x}_i(t),\boldsymbol{p}_i(t))$ can be calculated and (11) is estimated by

$$\langle O\rangle(t) = \frac{1}{N}\sum_{i=1}^{N} O(\boldsymbol{x}_i(t),\boldsymbol{p}_i(t)). \quad (12)$$

The classical equations of motion have to be solved for a sufficient large sample of members from this ensemble.

The nonrelativistic version of the phase-space averaging method has been introduced by Percival *et al.* [21] in order to study the charge transfer and ionization of hydrogen ions by protons and the ionization of highly excited atoms by electric fields. It has been utilized in various studies of light-matter interaction, see [15] for a short review. Here, we will apply this method to light-matter interaction in the relativistic regime [22,27]. A fully relativistic phase-space averaging method for the three-dimensional electron motion in hydrogen atoms ($Z = 1$) has been introduced in [22]. In this section, we are going to review and to extend this method. Generalizing [22] we will consider single-electron motion in a three-dimensional Coulomb potential with $Z \geqslant 1$ and we show how to adopt the relativistic phase-space averaging method for general central potentials in one, two, and three dimensions.

Starting from the initial condition $(\boldsymbol{x}_0,\boldsymbol{p}_0)$, we obtain the single-particle trajectories by integrating the equations of motion

$$\frac{d\boldsymbol{x}(t)}{dt} = \frac{\boldsymbol{p}(t)}{m\sqrt{1+\frac{\boldsymbol{p}(t)^2}{m^2c^2}}}, \quad (13a)$$

$$\frac{d\boldsymbol{p}(t)}{dt} = -e\left(\boldsymbol{E}(\boldsymbol{x}(t),t) + \frac{\boldsymbol{p}(t)\times\boldsymbol{B}(\boldsymbol{x}(t),t)}{m\sqrt{1+\frac{\boldsymbol{p}(t)^2}{m^2c^2}}}\right) \quad (13b)$$

numerically by means of an implicit Runge-Kutta method. The electromagnetic fields $\boldsymbol{E}(\boldsymbol{x},t)$ and $\boldsymbol{B}(\boldsymbol{x},t)$ are given by the superposition of the external laser field (2) and one of the central potentials (4) or (5):

$$\boldsymbol{E}(\boldsymbol{x},t) = \boldsymbol{E}_L(\boldsymbol{x}-\boldsymbol{x}_0,t) + \frac{1}{e}\nabla V(|\boldsymbol{x}|), \quad (14a)$$

$$\boldsymbol{B}(\boldsymbol{x},t) = \boldsymbol{B}_L(\boldsymbol{x}-\boldsymbol{x}_0,t). \quad (14b)$$

After the laser pulse has passed the electron, we determine whether it has been ionized or not. It has been ionized if its energy (16) exceeds mc^2, otherwise it remains bounded.

Solving the equations of motion (13) is computationally less demanding than solving the time-dependent Dirac (6) or Klein-Gordon (7) equation. It is not required to restrict the dynamics to two dimensions to keep the computing time manageable. Thus, the relativistic phase-space averaging method is a feasible scheme that enables us to investigate ionization of hydrogenlike ions in short intense laser pulses with the full three-dimensional Coulomb potential in a reasonable amount of computing time.

The preparation of the initial position $\boldsymbol{x}_0$ and the initial momentum $\boldsymbol{p}_0$ is a crucial step in the application of the phase-space averaging method. Initial conditions $(\boldsymbol{x}_0,\boldsymbol{p}_0)$ have to be sampled from a microcanonical ensemble with the uniform probability density

$$\varrho(\boldsymbol{x}_0,\boldsymbol{p}_0) \sim \delta(W - W(\boldsymbol{x}_0,\boldsymbol{p}_0)), \quad (15)$$

where W denotes the microcanonical ensemble's total energy. For a relativistic particle moving in a central potential $V(|\boldsymbol{x}|)$, the energy is given by

$$W(\boldsymbol{x},\boldsymbol{p}) = V(|\boldsymbol{x}|) + c\sqrt{m^2c^2+\boldsymbol{p}^2}. \quad (16)$$

Sampling the initial conditions from a nonuniform distribution leads to biased expectation values of observables [28]. The preparation of the initial conditions depends on the potential. In Newtonian mechanics as well as in relativistic mechanics [29] it is possible to devise analytic expressions for the classical trajectories in the Coulomb potential which allow one to devise a direct-sampling method to sample from (15). For general central potentials as soft-core potentials (5) we will apply a Markov chain Monte Carlo method that we will introduce in Sec. II C 2.

1. Coulomb potential

We consider bound electrons in a Coulomb field (4) with the energy

$$W = mc^2\sqrt{1-\alpha^2/(\hbar^2c^2)} \quad (17)$$

that equals the ground-state energy of the Dirac equation Coulomb problem. A relativistic particle of mass m in a Coulomb/Kepler potential (4) with energy $0 < W < mc^2$ and angular momentum $\alpha/c \leqslant L \leqslant \alpha/[c\sqrt{1-W^2/(m^2c^4)}]$ rotates in a bound rosette around the center of force [22,29]. The extremal radii are given by

$$r_{\min} = \bar{r} - \Delta r, \qquad r_{\max} = \bar{r} + \Delta r \quad (18)$$

with the Z-dependent relativistic Bohr radius

$$\bar{r} = \frac{W\alpha}{m^2c^4 - W^2} \quad (19a)$$

and

$$\Delta r = \frac{mc^2\alpha}{m^2c^4 - W^2}\sqrt{\frac{W^2}{m^2c^4} - \left(1-\frac{W^2}{m^2c^4}\right)\left(\frac{L^2c^2}{\alpha^2}-1\right)}. \quad (19b)$$

Because of the potential's rotational symmetry and the conservation of the angular momentum, the trajectory remains in a two-dimensional plane. Assuming that the particle is at

$t = 0$ in its pericenter [30], the trajectory may be parametrized in polar coordinates by a parameter u, viz.,

$$r(u) = \bar{r} - \Delta r \cos u, \tag{20a}$$

$$\varphi(u) = \frac{2}{\sqrt{1 - \frac{\alpha^2}{L^2c^2}}} \left\{ \arctan\left[\left(\frac{1 - \frac{W^2}{m^2c^4}}{\frac{L^2c^2}{\alpha^2} - 1} \right)^{1/2} \times \frac{mc^2(\bar{r} + \Delta r)}{\alpha} \tan\frac{u}{2} \right] + \left\lfloor \frac{u + \pi}{2\pi} \right\rfloor \pi \right\}, \tag{20b}$$

$$t(u) = \frac{\alpha}{mc^3\left(1 - \frac{W^2}{m^2c^4}\right)^{3/2}} u - \frac{mc\left(1 - \frac{W^2}{m^2c^4}\right)^{1/2} \bar{r}\Delta r}{\alpha} \sin u. \tag{20c}$$

The notation $\lfloor \cdot \rfloor$ denotes rounding to the largest integer not greater than the argument. The parameter u is a relativistic generalization of the eccentric anomaly of the nonrelativistic Kepler problem.

One can show [22] that in the microcanonical ensemble of the three-dimensional Coulomb potential the distribution of the squared angular momentum is uniform. Thus, the ensemble of initial conditions that corresponds to an electron in the ground state of a hydrogenlike ion having the total energy (17) can be parametrized by a set of five *uniformly* distributed *independent* random variables. These variables are the time $\hat{t}$, the squared angular momentum $\hat{L}^2$, and three Euler angles $\hat{\phi}$, $\hat{\theta}$, and $\hat{\psi}$. Sampling from the microcanonical ensemble is a four-step procedure:

(1) We choose a point in time $\hat{t}$ between two pericenters,

$$0 \leqslant \hat{t} < \frac{2\pi\alpha m^2c^3}{(m^2c^4 - W^2)^{3/2}} = \frac{2\pi\hbar^3}{m\alpha^2}, \tag{21}$$

and compute the eccentric anomaly u by solving the Kepler equation (20c).

(2) We select a random absolute value of the angular momentum, with

$$\frac{\alpha}{c} \leqslant \hat{L} \leqslant \hbar, \tag{22}$$

which determines together with u the radius (20a) and the angle (20b) of a point $(\hat{x}, \hat{y}, 0)$ in the x-y plane. Note that for the three-dimensional Coulomb potential, $\hat{L}$ has to be drawn such that $\hat{L}^2$ has uniform distribution.

(3) To identify the initial position $\boldsymbol{x}_0$ and the angular momentum $\boldsymbol{L}$, the point $(\hat{x}, \hat{y}, 0)$ and the vector $(0, 0, \hat{L})$ are rotated by three random Euler angles

$$0 \leqslant \hat{\phi} < 2\pi, \quad 0 \leqslant \hat{\theta} < 2\pi, \quad 0 \leqslant \hat{\psi} < 2\pi \tag{23}$$

about the z axis, the new x axis, and the new z axis, in this particular order.

(4) The initial momentum $\boldsymbol{p}_0$ follows from the conservation of the energy and the angular momentum,

$$\boldsymbol{p}_0 = \frac{\boldsymbol{L} \times \boldsymbol{x}_0}{|\boldsymbol{x}_0|^2} - \frac{\boldsymbol{x}_0}{|\boldsymbol{x}_0|} \sqrt{\left(\frac{W}{c} + \frac{\alpha}{|\boldsymbol{x}_0|c} \right)^2 - (mc)^2 - \left(\frac{\boldsymbol{L} \times \boldsymbol{x}_0}{|\boldsymbol{x}_0|^2} \right)^2}. \tag{24}$$

In the second step of the preparation of the initial condition, we assure that the initial position and momentum are such that $L = |\boldsymbol{x}_0 \times \boldsymbol{p}_0| \geqslant \alpha/c$ because trajectories of particles in a Coulomb field with an angular momentum $L < \alpha/c$ are unstable [29].

While propagating a single-particle trajectory from the initial condition $(\boldsymbol{x}_0, \boldsymbol{p}_0)$, the external laser field breaks the rotational symmetry of the Coulomb potential and, therefore, the angular momentum is no longer conserved and may become so small that the electron eventually falls into the nucleus. In this case, we have to reject the trajectory as unphysical [22]. Rejected trajectories do not contribute to the expectation values (12).

2. *General central potentials*

For general central potentials $V(|\boldsymbol{x}|)$ we implemented sampling from the microcanonical ensemble by Markov chains [31] which have been inspired by molecular dynamics methods [32]. The Markov chains generate sequences of initial conditions $(\boldsymbol{x}_{0,i}, \boldsymbol{p}_{0,i})$ by proposing new initial conditions $(\boldsymbol{x}_{0,\mathrm{new}}, \boldsymbol{p}_{0,\mathrm{new}})$ and setting $(\boldsymbol{x}_{0,i+1}, \boldsymbol{p}_{0,i+1}) = (\boldsymbol{x}_{0,i}, \boldsymbol{p}_{0,i})$ or $(\boldsymbol{x}_{0,i+1}, \boldsymbol{p}_{0,i+1}) = (\boldsymbol{x}_{0,\mathrm{new}}, \boldsymbol{p}_{0,\mathrm{new}})$ depending on the Metropolis-Hastings transition probability that is a function of the last initial condition $(\boldsymbol{x}_{0,i}, \boldsymbol{p}_{0,i})$ and the proposed one $(\boldsymbol{x}_{0,\mathrm{new}}, \boldsymbol{p}_{0,\mathrm{new}})$.

Note that Markov chains could also be used in the case of the Coulomb potential; however, in contrast to the direct-sampling method as described in Sec. II C 1, the Markov chain generates correlated initial conditions $(\boldsymbol{x}_{0,i}, \boldsymbol{p}_{0,i})$. For this reason, one has to perform a sufficiently large number of steps $j - i$ in the Markov chain, between two pairs $(\boldsymbol{x}_{0,i}, \boldsymbol{p}_{0,i})$ and $(\boldsymbol{x}_{0,j}, \boldsymbol{p}_{0,j})$ that are actually used as initial conditions for propagation in the laser field. Empirically we found that performing 64 steps in the Markov chain between two initial conditions was enough to reduce correlations sufficiently to perform ionization studies for the soft-core potential.

(a) One-dimensional potentials. For a one-dimensional potential the microcanonical distribution (15) reads

$$\varrho(x, p) \sim \delta(W - V(x) - \sqrt{m^2c^4 + c^2p^2}) \tag{25}$$

and the marginal distribution $\varrho(x)$ follows as

$$\varrho(x) \sim \int \delta(W - V(x) - \sqrt{m^2c^4 + c^2p^2})\, dp \sim \frac{1}{c}\left[1 - \left(\frac{mc^2}{W - V(x)} \right)^2 \right]^{-1/2}. \tag{26}$$

The support of $\varrho(x)$ is wherever $W - V(x) \geqslant mc^2$; for positions x with $W - V(x) < mc^2$ we define $\varrho(x) = 0$. The Markov chain starts with some position $x_{0,0}$ with $\varrho(x_{0,0}) > 0$.

In each step it samples $x_{0,\mathrm{new}}$ with uniform distribution from the support of $\varrho(x)$. New initial positions $x_{0,i+1}$ are given by

$$x_{0,i+1} = \begin{cases} x_{0,\mathrm{new}} & \text{with probability } \min\left(1, \frac{\varrho(x_{0,\mathrm{new}})}{\varrho(x_{0,i+1})}\right), \\ x_{0,i} & \text{with probability } 1 - \min\left(1, \frac{\varrho(x_{0,\mathrm{new}})}{\varrho(x_{0,i+1})}\right). \end{cases} \tag{27}$$

To each initial position $x_{0,i}$ belongs an initial momentum $p_{0,i}$ that is determined by the total energy W and the position $x_{0,i}$ and equals

$$p_{0,i} = \pm\frac{1}{c}\sqrt{[W - V(x_{0,i})]^2 - m^2c^4} \tag{28}$$

with equal probability.

(b) Two- and three-dimensional potentials. Markov chains to sample from microcanonical ensembles of two- and three-dimensional central potentials may be devised by the following considerations concerning the distribution of the angular momentum of a relativistic particle. The microcanonical probability of finding a particle at distance r moving in a three-dimensional central potential $V(|\boldsymbol{x}|)$ having squared angular momentum L^2 and energy W is given by

$$\begin{aligned} \varrho(L^2,r) &\sim (4\pi)^2 \int_0^\infty \int_{-1}^1 \delta(L^2 - r^2p^2(1-\mu^2)) \\ &\quad \times \delta(W - V(r) - c\sqrt{m^2c^2 + p^2})\varrho(\mu)r^2p^2\,d\mu\,dp \\ &\sim \frac{(4\pi)^2}{2c}\left(1 - \frac{L^2}{r^2\left(\frac{[W-V(r)]^2}{c^2} - (mc)^2\right)}\right)^{-1/2} \\ &\quad \times\left(1 - \left(\frac{mc^2}{W - V(r)}\right)^2\right)^{-1/2}, \end{aligned} \tag{29}$$

where $\varrho(\mu) = 1/2$ denotes the distribution of the cosine μ of the angle between two randomly chosen three-dimensional unit vectors. For two-dimensional systems, we find the joint probability distribution of the angular momentum L and the distance r:

$$\begin{aligned} \varrho(L,r) &\sim (2\pi)^2 \int_0^\infty \int_{-1}^1 \delta(L - rp\sqrt{1-\mu^2}) \\ &\quad \times \delta(W - V(r) - c\sqrt{m^2c^2 + p^2})\varrho(\mu)rp\,d\mu\,dp \\ &\sim \frac{(2\pi)^3}{c}\left(1 - \frac{L^2}{r^2\left(\frac{[W-V(r)]^2}{c^2} - (mc)^2\right)}\right)^{-1/2} \\ &\quad \times\left(1 - \left(\frac{mc^2}{W - V(r)}\right)^2\right)^{-1/2}, \end{aligned} \tag{30}$$

where $\varrho(\mu) = \pi/\sqrt{1-\mu^2}$ denotes the distribution of the cosine μ of the angle between two randomly chosen two-dimensional unit vectors. Note that the right-hand sides of (29) and (30) share—up to a constant factor—the same algebraic form, but for three-dimensional systems the distribution (29) is a function of the squared angular momentum whereas (30) is a function of the angular momentum for two-dimensional systems. For the following considerations it will be convenient to define $\varrho(L^2,r) = 0$ and $\varrho(L,r) = 0$ if one of the arguments of the square roots in (29) and (30) is negative.

For three-dimensional central potentials the Markov chain generates a sequence of pairs (L_i^2,r_i) starting from some (L_0^2,r_0) with $\varrho(L_0^2,r_0) > 0$ and the transition rule

$$\begin{aligned} &\left(L_{i+1}^2,r_{i+1}\right) \\ &= \begin{cases} \left(L_{\mathrm{new}}^2,r_{\mathrm{new}}\right) & \text{with probability } \min\left(1, \frac{\varrho(L_{\mathrm{new}}^2,r_{\mathrm{new}})}{\varrho(L_i^2,r_i)}\right), \\ \left(L_i^2,r_i\right) & \text{with probability } 1 - \min\left(1, \frac{\varrho(L_{\mathrm{new}}^2,r_{\mathrm{new}})}{\varrho(L_i^2,r_i)}\right). \end{cases} \end{aligned} \tag{31}$$

New pairs $(L_{\mathrm{new}}^2,r_{\mathrm{new}})$ are proposed by sampling uniformly from the support of $\varrho(L^2,r)$. Each pair (L_i^2,r_i) translates into an initial condition $(\boldsymbol{x}_{0,i},\boldsymbol{p}_{0,i})$ by rotating the vectors $(r_i,0,0)$ and $(p_i\cos\beta_i, p_i\sin\beta_i,0)$ by three random Euler angles

$$0 \leqslant \hat{\phi} < 2\pi, \quad 0 \leqslant \hat{\theta} < 2\pi, \quad 0 \leqslant \hat{\psi} < 2\pi \tag{32}$$

about the z axis, the new x axis, and the new z axis, in this particular order. The momentum p_i and the angle β_i are determined by the radius and the angular momentum as

$$p_i = \sqrt{\left(\frac{W - V(r_i)}{c}\right)^2 - (mc)^2}, \tag{33}$$

$$\beta_i = \arcsin\frac{L_i}{r_i\,p_i}. \tag{34}$$

The Markov chain for sampling from the microcanonical ensemble of two-dimensional central potentials works similarly to the three-dimensional case. However, it produces a sequence of pairs (L_i,r_i), such that

$$\begin{aligned} &(L_{i+1},r_{i+1}) \\ &= \begin{cases} (L_{\mathrm{new}},r_{\mathrm{new}}) & \text{with probability } \min\left(1, \frac{\varrho(L_{\mathrm{new}},r_{\mathrm{new}})}{\varrho(L_i,r_i)}\right), \\ (L_i,r_i) & \text{with probability } 1 - \min\left(1, \frac{\varrho(L_{\mathrm{new}},r_{\mathrm{new}})}{\varrho(L_i,r_i)}\right), \end{cases} \end{aligned} \tag{35}$$

and new pairs $(L_{\mathrm{new}},r_{\mathrm{new}})$ are proposed by sampling uniformly from the support of $\varrho(L,r)$. The proposed angular momentum L_{new} may be positive or negative allowing for different rotational directions. Initial conditions $(\boldsymbol{x}_{0,i},\boldsymbol{p}_{0,i})$ are given by rotating $(r_i,0,0)$ and $(p_i\cos\beta_i, p_i\sin\beta_i,0)$ by a random Euler angle $0 \leqslant \hat{\phi} < 2\pi$ about the z axis.

III. RELATIVISTIC QUANTUM DYNAMICS VERSUS RELATIVISTIC PHASE-SPACE AVERAGING

As outlined in Sec. II B it is computationally too demanding to simulate the full relativistic quantum dynamics in three dimensions by solving the time-dependent Dirac or Klein-Gordon equation. For three-dimensional systems we will have to rely on the relativistic phase-space averaging method. Note that classical trajectory Monte Carlo methods may be extended to incorporate quantum features [33], yet requiring averages over significantly more trajectories for convergence. There is a trade-off between accounting for quantum effects and computational feasibility.

The phase-space averaging method may be an adequate approximation for Rydberg states in the case of low laser

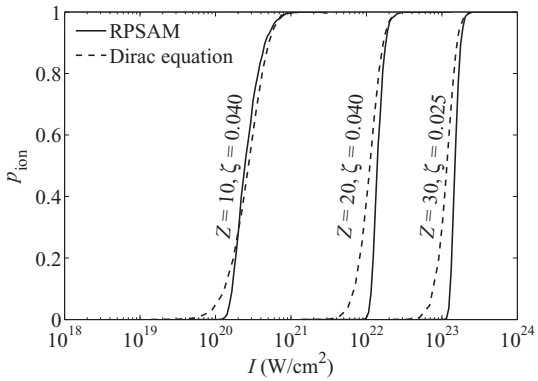

FIG. 2. Ionization probability $p_{\rm ion}$ as a function of the laser intensity I for an electron in a two-dimensional soft-core potential (5) calculated by two different computational approaches: the solution of the time-dependent Dirac equation and the relativistic phase-space averaging method (RPSAM). Calculations are performed with different atomic numbers Z. Soft-core parameters ζ were chosen such that the ground-state energy equals the ground-state energy of the Coulomb potential with the same Z. In all cases, the laser field is made up of a pulse with envelope $w_{\rm rect}(\eta,2)$ and has a wavelength of $\lambda = 6.5$ nm.

frequencies [34]. For the hydrogen atom it was found that quantum and classical simulations [35] agree quite well for a laser frequency of $\omega = 2 \times 10^{15}\,{\rm s}^{-1}$ with intensities above the atomic unit intensity of $I = 3.5 \times 10^{16}\,{\rm W/cm}^2$. Classical trajectory Monte Carlo simulations have been applied in many studies, e.g., the investigation of microwave ionization of atoms or the analysis of stabilization [36] of hydrogenlike ions below an atomic number of $Z = 10$ [27] and for acceleration studies of electrons up to giga-electron-volt energies [37].

However, as a classical approach, the (relativistic) phase-space averaging method is not able to cover genuine quantum mechanical features, e.g., tunneling. Thus, we estimated the systematic error that is caused by modeling the ionization dynamics via the phase-space averaging method by comparing the relativistic quantum dynamics with the classical relativistic phase-space averaging method in one and two dimensions. More precisely, we determined the ionization probability $p_{\rm ion}$ for an electron in a two-dimensional soft-core potential (5) by means of the numerical solution of the Dirac equation and the Klein-Gordon equation as well as by the relativistic phase-space averaging method. In Fig. 2 we show the ionization probability $p_{\rm ion}$ as a function of the mean laser intensity

$$I = \tfrac{1}{2} c \varepsilon_0 E_{L,\max}^2 \tag{36}$$

for the Dirac equation as well as for the relativistic phase-space averaging method. Here we consider two-dimensional soft-core potentials (5) with different atomic numbers Z and lasers with a wavelength of $\lambda = 6.5$ nm. We find a reasonable match of the ionization probabilities especially in the over-the-barrier ionization regime of high ionization probabilities. In the regime of intensities well below the classical ionization potential ionization probabilities are low because ionization happens via tunneling (tunneling regime). In the tunneling regime the relativistic phase-space averaging method underestimates the ionization probability, because tunneling is inherently neglected. Once energies above the classical ionization potential are imposed (above-the-barrier-ionization) both methods tend to agree better. The discrepancy between the quantum mechanical ionization probability and the ionization probability as obtained by the relativistic phase-space averaging method (classical ionization) depends also on the wavelength and the system's dimension.

To study the wavelength dependence of the ionization probability we have to employ the Klein-Gordon equation in order to reduce the numerical computation time. The discrepancy between the quantum mechanical ionization probability and the classical ionization probability increases as we go to larger wavelengths, shown in Fig. 3. As the wavelength increases, the electron has more time to tunnel through the potential barrier. The increasing shift of the ionization profile of the quantum mechanical calculations toward lower intensities indicates that tunneling becomes more and more important for larger wavelengths till it completely dominates the ionization process.

Because of tunneling one may expect that the quantum mechanical ionization probability *always* exceeds the classical ionization probability. For very short wavelengths, however, we find that classical ionization probabilities may be larger than the quantum mechanical ones. For example, for $\lambda =$ 5 nm and small intensities classical ionization probabilities are smaller than quantum mechanical ionization probabilities because of tunneling, see Fig. 3. For larger intensities, however, we observe signatures of above-the-barrier reflection [38] reducing the quantum mechanical ionization as compared to classical ionization.

The comparison between the left column and the right column of Fig. 3 illustrates the impact of the dimension on the quality of the match between the quantum mechanical ionization probability and the classical ionization probability. The left column shows the wavelength dependence of the ionization probability for one-dimensional systems where quantitative differences between the two approaches are rather large. The intensities at which the ionization profiles reach $p_{\rm ion} = 0.5$ differ by a factor of 3.9, 2.6, and 1.1, respectively, for the setups in the left column of Fig. 3. Quantum and classical calculations agree better if we consider the ionization dynamics in two dimensions, as shown in the right column of Fig. 3. Here, the relativistic phase-space averaging method is a reasonable approximation for the employed laser wavelengths. The intensities at which the ionization profiles reach $p_{\rm ion} = 0.5$ differ only by a factor of 2.3, 1.5, and 1.1, respectively. Extrapolating dimensional effects we presume that in three dimensions the role of quantum effects is reduced further.

Thus, we conclude that the relativistic phase-space averaging method is a useful approach to study ionization of hydrogenlike ions in ultrastrong few-cycle laser pulses of wavelengths in the range from the near-infrared to soft x-ray radiation. Our comparison of the relativistic phase-space averaging method with the solution of the Klein-Gordon equation demonstrates that ionization profiles as obtained by the relativistic phase-space averaging method may be utilized to determine the peak laser intensity of intense few-cycle laser pulses having wavelengths in the range from near-infrared to soft x-ray radiation by the ionization yield with a systematic error of a factor of about two. QED effects via laser-induced vacuum polarization, which may demand further corrections, can be neglected because the laser intensities as considered

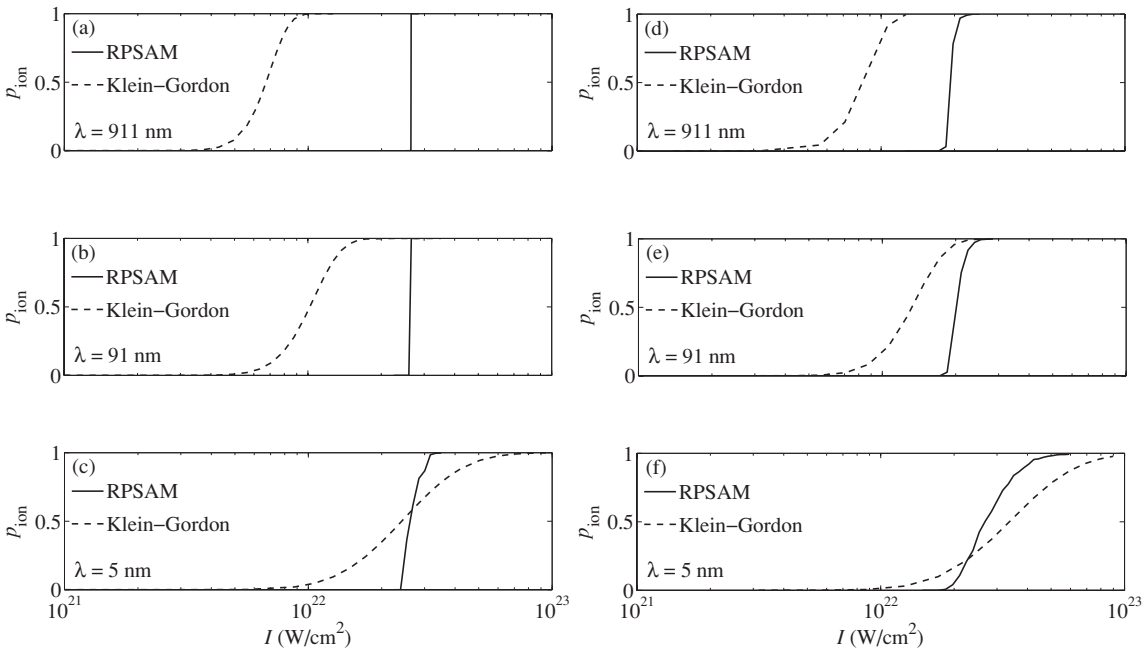

FIG. 3. Ionization probability $p_{\rm ion}$ as a function of the laser intensity I for an electron in a one-dimensional soft-core potential (left column) and in a two-dimensional soft-core potential (right column) calculated by two different computational approaches: the solution of the time-dependent Klein-Gordon equation and the relativistic phase-space averaging method (RPSAM). Calculations are performed with the atomic number $Z = 20$ and the soft-core parameters $\zeta = 0.06$ (one-dimensional soft-core potential) and $\zeta = 0.032$ (two-dimensional soft-core potential). In all cases, the laser field is made up of a pulse with envelope $w_{\rm rect}(\eta,1)$. Wavelengths lie in the near-infrared ($\lambda = 911$ nm), in the ultraviolet ($\lambda = 91$ nm), and in the soft x-ray range ($\lambda = 5$ nm).

in this contribution are high but still far below the Schwinger intensity of about 10^{29} W/cm^2. QED corrections in heavy ions may be substantial for systems with $Z \gtrapprox 50$ only [39].

IV. RELATIVISTIC IONIZATION OF HYDROGENLIKE IONS

The ionization of hydrogenlike ions in intense laser fields depends in a complex manner on the atomic number, the laser frequency, the electric field strength, the pulse length, and the shape of the pulse. In this section, we investigate relativistic ionization in various laser setups as available today or in the near future. In doing so we focus on the ionization probability and study the dynamics of the electron probability density.

A. Dynamics of the electron probability density—quantum mechanical studies

In Fig. 4 we present the two-dimensional quantum mechanical evolution of the electron probability density during the ionization of an electron in a soft-core potential (5) with $Z = 10$, $\zeta = 0.079a_0$, and a_0 denoting the Bohr radius. The laser pulse has a wavelength of $\lambda = 17.6$ nm and a peak field strength of $E_{L,\rm max} = 5.14 \times 10^{13}$ V/m corresponding to an average intensity of 3.52×10^{20} W/cm^2, and the envelope

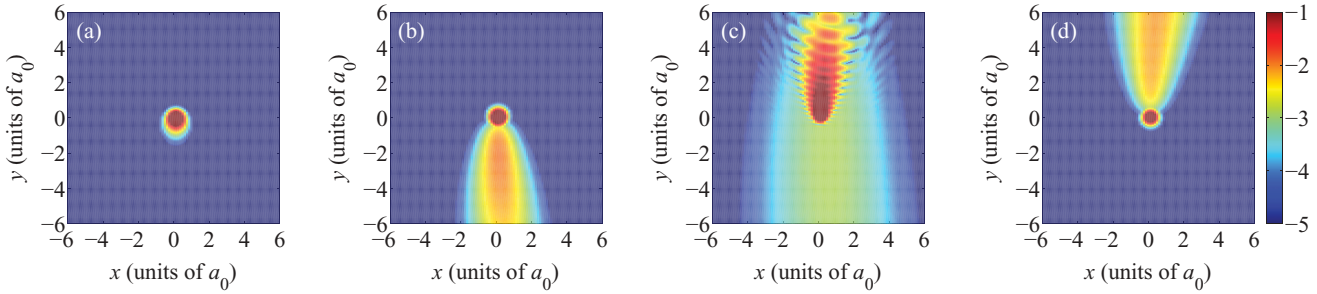

FIG. 4. (Color online) Snapshots of the Dirac electron probability density for an electron in a soft-core potential (5) with $Z = 10$ and $\zeta = 0.079a_0$ on a logarithmic scale for a field strength of $E_{L,\rm max} = 5.14 \times 10^{13}$ V/m corresponding to an average intensity of 3.52×10^{20} W/cm^2 at different points in time: (a) $t = 1/4\,T$, (b) $t = 2/4\,T$, (c) $t = 3/4\,T$, and (d) $t = 4/4\,T$, with $T = \lambda/c$ and $\lambda = 17.6$ nm. Length scales of the propagation direction (x axis) and the polarization direction (y axis) are given in units of the Bohr radius a_0; the pulse shape is formed by the envelope function $w_{\rm ramp}(\eta,4,1)$.

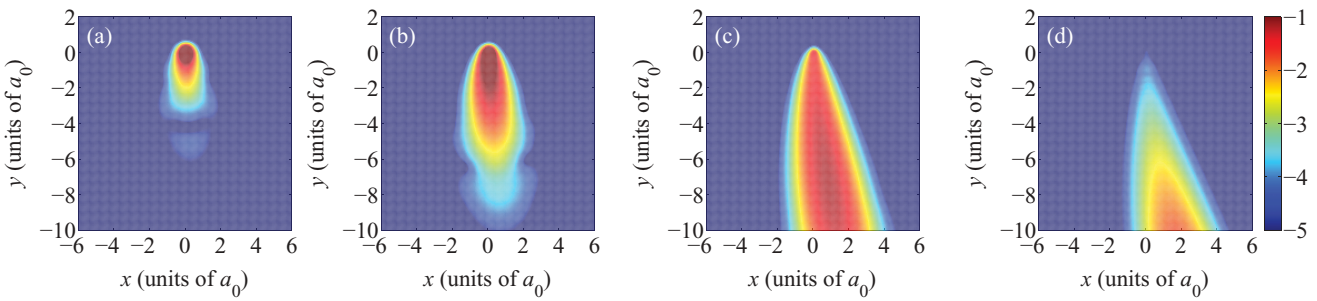

FIG. 5. (Color online) Snapshots of the Dirac electron probability density for an electron in a soft-core potential (5) with $Z = 10$ and $\zeta = 0.079a_0$ on a logarithmic scale for various field strengths and intensities, respectively: (a) $E_{L,\max} = 3.07 \times 10^{13}$ V/m, $I = 1.25 \times 10^{20}$ W/cm^2; (b) $E_{L,\max} = 5.14 \times 10^{13}$ V/m, $I = 3.51 \times 10^{20}$ W/cm^2; (c) $E_{L,\max} = 1.03 \times 10^{14}$ V/m, $I = 1.41 \times 10^{21}$ W/cm^2; (d) $E_{L,\max} = 1.54 \times 10^{14}$ V/m, $I = 3.15 \times 10^{21}$ W/cm^2. The snapshots were taken at $T/4$ with $T = \lambda/c$ and $\lambda = 17.6$ nm, length scales are given in units of the Bohr radius a_0, and the pulse shape is formed by the envelope function $w_{\text{rect}}(\eta,2)$.

function is given by $w_{\text{ramp}}(\eta,4,1)$. The figure shows the probability density when the first maximum [Fig. 4(a)], the first minimum [Fig. 4(b)], the second maximum [Fig. 4(c)], and the second minimum [Fig. 4(d)] of the electric field strength passes the ionic core. During the first half-period of the laser cycle—the turn-on ramp—the electric force points in the negative y direction and the electron gains momentum in the same direction, whereas in the second half-period, the electric force points in the opposite direction, deaccelerating the electron and causing distinct interference patterns by scattering on the ionic core [40], as shown in Fig. 4(c). The electric field strength of the setup in Fig. 4 is large enough to accelerate the electron to velocities comparable with the speed of light so that the magnetic field component of the Lorentz force becomes relevant and accelerates the electron into the propagation direction of the laser pulse.

The effect of the Lorentz force, which grows with increasing laser field, is visualized in Fig. 5. Here, we compare the electron density at time $t = \lambda/(4c)$—when the first maximum of the electromagnetic field is passing the ionic core—for four different laser field strengths $E_{L,\max}$ having the same laser wavelength $\lambda = 17.6$ nm and envelope function $w_{\text{rect}}(\eta,2)$. For a laser field strength of $E_{L,\max} = 3.07 \times 10^{13}$ V/m well below the mean atomic field strength of an electron on the first Bohr orbit of $Z = 10$, the effect of the Lorentz force is marginal, see Fig. 5(a). However, at higher field strengths, the Lorentz force accelerates the electron into the propagation direction resulting in an asymmetric distribution of the electron probability distribution as shown in Fig. 5(d).

B. Ionization probability—classical studies

In this section, we are going to investigate the ionization probability of hydrogenlike ions in intense laser fields as a function of the electric field strength, the atomic number, the laser frequency, and the pulse shape by means of the classical relativistic phase-space averaging technique, as described in Sec. II C, taking into account the full three-dimensional Coulomb potential.

1. Ionization profiles, scaling relations, and relativistic effects

Before we examine the influence of some laser parameters on the ionization probability, we characterize the basic features of a typical ionization profile for a single-cycle rectangular laser pulse. Shifting from the infrared regime which has been considered in [12] to the soft x-ray regime, Fig. 6 illustrates the ionization probability p_{ion} as a function of the electric field strength $E_{L,\max}$ and the mean laser intensity I for hydrogenlike ions with different nuclear charges Z [41] in a laser pulse with fixed wavelength $\lambda = 6.5$ nm. The ionization profiles show a typical threshold behavior. At intensities below some critical value, the ionization probability is zero, above this critical intensity, the ionization probability rises rapidly and saturates for intensities considerably above the critical intensity. The maximal slope of the ionization profile is essential to determine the laser intensity, as described in [12]. The ionization profiles for $Z \geqslant 35$ in Fig. 6 show some kinks as indicated by black arrows. These kinks correspond to changes in the decay rate of $1 - p_{\text{ion}}$ which we will investigate in Sec. IV B 2.

In the nonrelativistic limit ionization profiles obey a simple scaling relation. The breakdown of this scaling relation

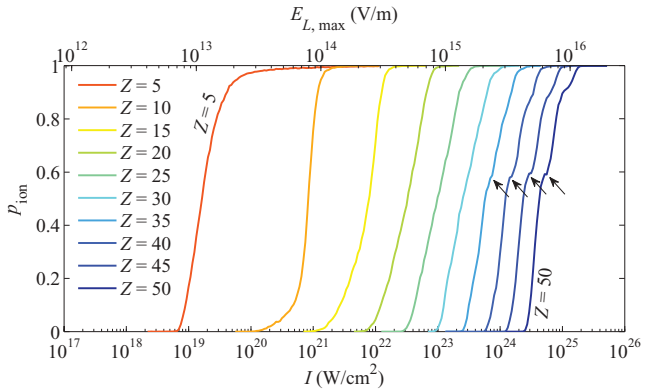

FIG. 6. (Color online) Ionization probability as a function of the mean laser intensity I and the maximal electric field strength $E_{L,\max}$ for hydrogenlike ions of different atomic numbers Z and a laser pulse with wavelength of $\lambda = 6.5$ nm. The atomic number Z increases from left to right. The pulse shape is formed by the envelope function $w_{\text{rect}}(\eta,2)$. Ionization profiles have been obtained by averaging over 10 000 trajectories or more per data point. Kinks in the ionization profiles correspond to changes in the decay rate of the occupation probability $1 - p_{\text{ion}}$, see Sec. IV B 2.

portends relativistic effects. The ionization dynamics of hydrogenlike ions in strong laser fields is affected by four independent system parameters: the nuclear charge Z, the laser wavelength λ, the laser's field amplitude $E_{L,\max}$, and the phase α_L. In the nonrelativistic limit, however, the equation of motion (13) obeys a scaling relation that allows us to reduce the number of independent system parameters by one. The nonrelativistic limit of (13) reads

$$\frac{d^2\boldsymbol{x}(t)}{dt^2} = -\frac{\alpha}{m}\frac{\boldsymbol{x}(t)}{|\boldsymbol{x}(t)|^3} - \frac{e}{m}\boldsymbol{E}_{L,\max} w(-\omega t, j)\sin(\alpha_L - \omega t), \quad (37)$$

provided that $|\boldsymbol{x}(t)| \ll \lambda$. If the wavelength is sufficiently large, $\lambda \gg \hbar^2/(\alpha m)$, the condition $|\boldsymbol{x}(t)| \ll \lambda$ is clearly satisfied before ionization occurs. The quantity $\hbar^2/(\alpha m)$ equals the Z-dependent (nonrelativistic) Bohr radius. Rescaling the Coulomb field strength, the space, the time, the laser frequency, and the laser field strength by

$$\alpha = Z\alpha', \quad \boldsymbol{x} = \frac{1}{Z}\boldsymbol{x}', \quad t = \frac{1}{Z^2}t', \quad \omega = Z^2\omega', \quad E_{L,\max} = Z^3 E'_{L,\max} \quad (38)$$

we obtain a new equation of motion

$$\frac{d^2\boldsymbol{x}'(t')}{dt'^2} = -\frac{\alpha'}{m}\frac{\boldsymbol{x}'(t')}{|\boldsymbol{x}'(t')|^3} - \frac{e}{m}\boldsymbol{E}'_{L,\max} w(-\omega' t')\sin(\alpha_L - \omega' t'), \quad (39)$$

where the dependence on the nuclear charge Z cancels out [42]. The new scale (38) implies a new laser wavelength λ' with $\lambda = \lambda'/Z^2$. Note that we have two different length scales—the wavelength and the electron's position—that scale differently. This is a consequence of not scaling the speed of light $c = \lambda\omega/(2\pi)$.

As as consequence of (39), one may expect that the ionization probability for a hydrogenlike ion with a (small) nuclear charge Z in a laser pulse with the electric field strength $E_{L,\max}$, the intensity I, and a wavelength of λ will be the same as for a hydrogen atom in a laser pulse with the same shape but with an electric field strength of $E_{L,\max}/Z^3$ (intensity of I/Z^6) and a wavelength of λ/Z^2. Figure 7 illustrates the probability *not* to ionize—the occupation probability—as a function of the scaled intensity I/Z^6 for hydrogenlike ions of different atomic numbers Z and a laser pulse with scaled wavelength of $\lambda = (1\ \mu m)/Z^2$. In all cases, the wavelength λ is several orders of magnitude larger than the relativistic Z-dependent Bohr radius (19a). For small Z, i. e., in the nonrelativistic limit, the ionization profiles collapse to a single curve if the occupation probability $1 - p_{\text{ion}}$ (or the ionization probability p_{ion}) is plotted against I/Z^6. In this regime the ionization threshold as obtained by the phase-space averaging method agrees quite well with the value $7.7 \times 10^{14}\,\text{W/cm}^2 \cdot Z^6$ that can be derived by a classical model of nonrelativistic quasistatic tunneling [43]. For larger Z, however, relativistic effects set in and the ionization profiles for hydrogenlike ions with large nuclear charge no longer coincide with the ionization profile of hydrogen. Ionization sets in at smaller scaled intensities I/Z^6 for large-Z nuclei. High-Z ionization profiles approach

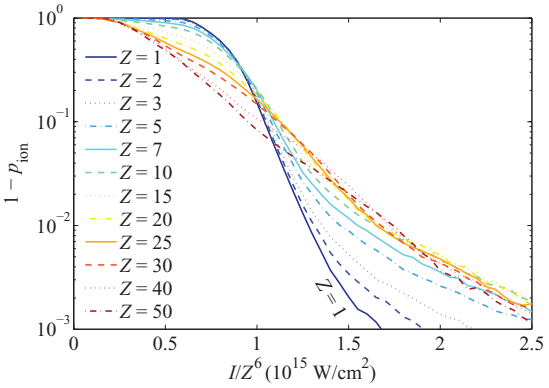

FIG. 7. (Color online) Occupation probability $1 - p_{\text{ion}}$ as a function of the scaled intensity I/Z^6 for hydrogenlike ions of different nuclear numbers Z and a laser pulse with scaled wavelength of $\lambda = (1\ \mu m)/Z^2$. Ionization profiles for small Z (nonrelativistic limit) collapse onto a universal curve; deviations from this curve are caused by relativistic effects. The pulse shape is formed by the envelope function $w_{\text{rect}}(\eta, 2)$. The noise in the tails of the distributions is due to the statistical uncertainties by the relativistic phase-space averaging method. Ionization profiles have been obtained by averaging over 50 000 trajectories per data point.

ionization probability one more slowly than low-Z ionization profiles. Thus relativistic effects lower the ionization threshold but reduce ionization rates at high intensities.

We find that for large Z and the laser parameters chosen here the ionization profile follows approximately an exponential decay law. Above some threshold intensity, the occupation probability falls exponentially as a function of the laser intensity I/Z^6 as shown in Fig. 7. For small Z, the occupation probability decays subexponentially. Figure 2 shows the ionization probability as obtained by solving the two-dimensional Dirac equation. If we plot the data of Fig. 2 on the same scale as in Fig. 7 (not shown), we find that this probability falls exponentially, too. Thus, both methods—the solution of the Dirac equation and the relativistic phase-space averaging method—make the same qualitative predictions.

Fraiman *et al.* [44] demonstrate that electron-ion collision in strong laser fields is also affected by the nonrelativistic dimensionless parameter $\epsilon = m^2\omega^4/(4\pi\varepsilon_0 e E^3_{L,\max})$. For $\epsilon > 1$ an ionized electron may be rescattered or trapped by the ionic core. All simulations in this contribution are carried out in the $\epsilon < 1$ regime, where rescattering plays a negligible role. To allow rescattering one has to apply higher laser frequencies. In particular, we apply laser frequencies that are much lower than the frequency $m\alpha^2/\hbar^3$ of the orbit of the ground state. Thus, ionization happens in a quasistatic regime.

2. *Influence of the laser wavelength on the ionization probability*

For simplicity and clarity, we investigate the effect of the laser wavelength on the ionization fraction for a one-cycle rectangular pulse without any additional field ramping. Thus, the pulse duration changes with the wavelength, but the number of electric field maxima remains constant. Figure 8 shows the probability $1 - p_{\text{ion}}$ measured at the end of a one-cycle sinusoidal pulse as a function of the mean laser intensity I for hydrogenlike ions with $Z = 30$, for intensities to be achieved

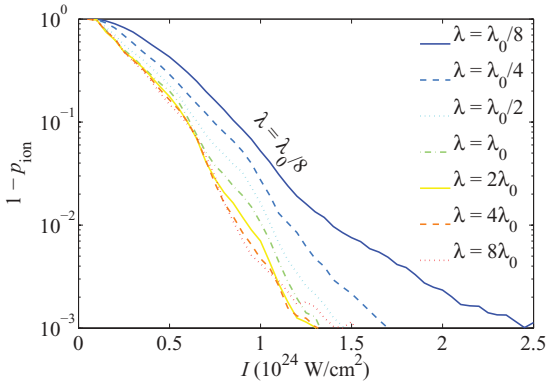

FIG. 8. (Color online) Occupation probability $1-p_{\rm ion}$ as a function of the intensity I for hydrogenlike ions with $Z=30$. The applied laser pulse has a shape function $w_{\rm rect}(\eta,2)$ and wavelengths of various multiples of $\lambda_0=6.5$ nm. The intensity range is expected to be accessible to high-intensity laser facilities of the near future.

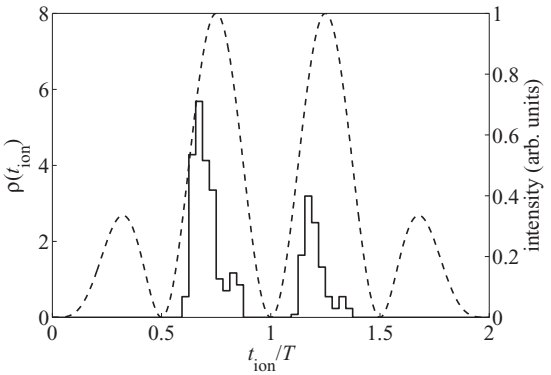

FIG. 9. Probability histogram $\rho(t_{\rm ion})$ of the moment of ionization for ionization of hydrogenlike ions with $Z=25$ in laser pulses of wavelength $\lambda=1054$ nm, peak field strength $E_{L,\max}=7\times10^{14}$ V/m, and intensity profile proportional to $[w_{\rm ramp}(\eta,4,1)\sin(\eta)]^2$ (solid line, left axis) and the intensity near the ionic core (dashed line, right axis). T denotes the laser period $T=\lambda/c$. Ionization happens most likely at the steepest intensity ascent.

in the near future. The laser's wavelength λ varies from the ultraviolet ($\lambda=52$ nm) [7] over the soft x-ray ($\lambda=6.5$ nm) [45] toward the hard x-ray ($\lambda=0.8$ nm) [46] range, by several multiples of the reference wavelength $\lambda_0=6.5$ nm.

We find for the relativistic phase-space averaging method applied to the three-dimensional Coulomb potential an exponential decay of the probability $1-p_{\rm ion}$ as a function of the intensity I. The decay rate grows with the wavelength λ. Smaller wavelengths lead to a reduction of the interaction time between the laser and the ion, which decreases the ionization probability for fixed intensities. The decay rate is for given λ and Z not constant over all intensities. Especially for long wavelengths, the ionization profile has intensity intervals with different decay rates. Note the kink in the semilogarithmic plot of $1-p_{\rm ion}$ for $\lambda=8\lambda_0$ in Fig. 8. For atomic numbers other than $Z=30$, we observe a qualitatively similar dependence of the ionization probability on the laser wavelength as for $Z=30$.

3. Moment of ionization

Let us define the electron's energy neglecting the contribution of the electromagnetic laser field by $W_{\rm free}(t)=W(\boldsymbol{x}(t),\boldsymbol{p}(t))$, where $\boldsymbol{x}(t)$ and $\boldsymbol{p}(t)$ denote the trajectory and the momentum of an classical electron in the relativistic phase-space averaging method and $W(\boldsymbol{x}(t),\boldsymbol{p}(t))$ is given by (16). For electrons that are eventually ionized, we call the first point in time where $W_{\rm free}(t)$ exceeds the electron's rest energy mc^2 the moment of ionization $t_{\rm ion}$.

Figure 9 shows the distribution $\rho(t_{\rm ion})$ of the moment of ionization for a laser pulse with an on-off-ramp and a maximal field strength such that $p_{\rm ion}\approx0.4$. Turn-on and turn-off half-cycles and bulk half-cycles differ in the maximum field strength as well as in the maximal rate of intensity change. To ionize, the electron has to accumulate energy from the external laser field, which is most efficient when the Hamiltonian—that is the external laser field—changes most rapidly. In fact, the ionization rate is highest when the intensity raises most rapidly, which is about an eighth-period before the global intensity maximum is reached. Note that the fast intensity increase allows ionization in the bulk half-cycles (second and third half-cycle) of the pulse in Fig. 9 at intensities smaller than the maximum intensity of the turn-on and turn-off half-cycles. Virtually no ionization occurs during the turn-on and turn-off phases.

4. Influence of the laser pulse shape on the ionization probability

The manipulation of the shape of a pulse is a capable tool to control ionization and to generate complex tailored pulses [47]. Besides the peak laser intensities, also the pulse shape of ultrashort and ultrastrong fields is experimentally challenging to measure and, therefore, a crucial parameter to be examined.

Laser pulses with the same wavelength and the same pulse energy may have different pulse shapes. An example of two such pulses is given in Fig. 10(a). Despite the fact that both pulses have the same energy, the ionic electron will not gather the same amount of energy from the two pulses with different shapes, which results in different ionization profiles as shown in Fig. 11. The ionization probability depends only indirectly on the pulse energy. It is primarily determined by the maximal rate of intensity increase and how often it is attained in the laser pulse.

The maximal rate of intensity increase is proportional to the peak intensity. To compare different pulse shapes with the same intensity maximum, we have chosen a ramp pulse with additional turn-on and turn-off phases and a smooth $\sin^2$-shaped envelope pulse; the corresponding intensities are presented in Figs. 10(b) and 10(c), respectively. The two pulses shown in Fig. 10(b) [and in Fig. 10(c)] have very similar intensity profiles in the pulse bulk but differ in their tails. For pulses with similar bulk intensity profiles, we find very similar ionization profiles, as plotted in Fig. 12. For the profiles $w_{\rm ramp}(\eta,6,2)$ and $w_{\sin^2}(\eta,16)$ the ionization profiles are virtually indistinguishable, and for $w_{\rm ramp}(\eta,3,1)$ and $w_{\sin^2}(\eta,3)$ the ionization profiles differ only marginally. Thus we conclude that the ionization profiles depend on the intensity maximum of a pulse and how often the maximum is attained but little on the details of the pulse tails. These findings are in accordance with the fact that ionization happens when the rate of intensity increase is maximal.

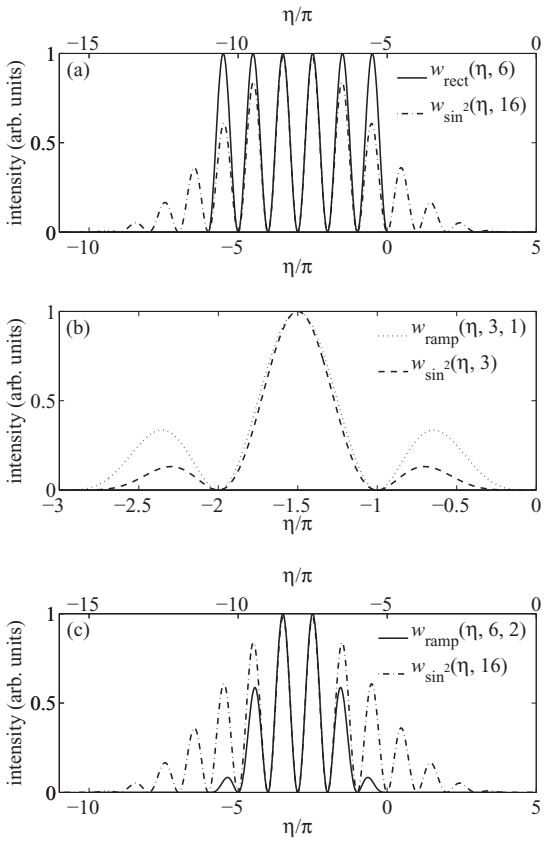

FIG. 10. (a) Pair of intensity profiles with the same pulse energy. (b), (c) Two pairs of laser pulses with similar intensity profile in the pulse's bulk but with different tails. For comparison of the laser pulses, the horizontal positions of the pulses in (a) and (c) have been shifted such that the pulse maxima are at the same position.

Experimental techniques allow to manipulate and control the electric field of ultrashort laser pulses by stabilizing the carrier phase α_L [48]. In Fig. 13 we show three intensity profiles with the same shape function $w_{\sin^2}(\eta,3)$ but different phases, and Fig. 14 depicts the corresponding ionization profiles. We find a marginal dependence of the ionization

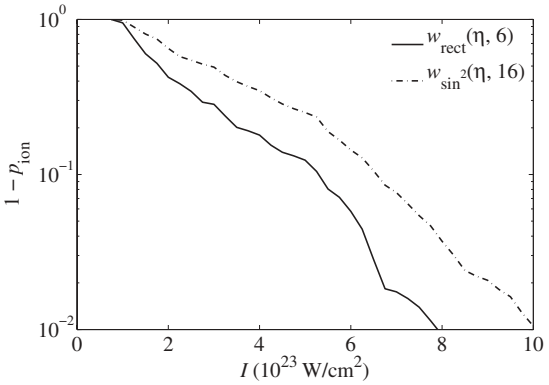

FIG. 11. Occupation probability $1 - p_{\mathrm{ion}}$ as a function of the intensity $I = c\varepsilon_0 E^2_{L,\max}/2$ for hydrogenlike ions with $Z = 30$ and laser pulses of wavelength $\lambda = 6.5$ nm and pulse shapes shown in Fig. 10(a). Laser pulses with same pulse energy but different intensity profiles result in distinct ionization profiles.

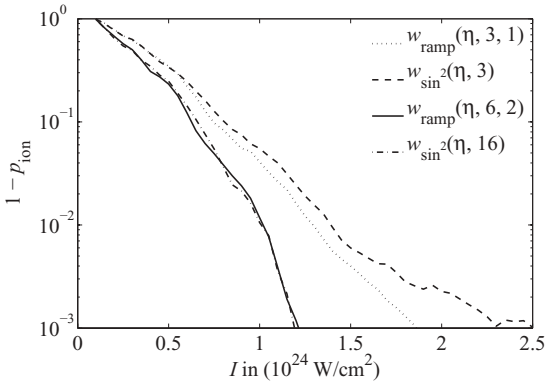

FIG. 12. Occupation probability $1 - p_{\mathrm{ion}}$ as a function of the intensity $I = c\varepsilon_0 E^2_{L,\max}/2$ for hydrogenlike ions with $Z = 30$ and laser pulses of wavelength $\lambda = 6.5$ nm and pulse shapes shown in Figs. 10(b) and 10(c). Laser pulses with similar intensity profiles in the pulse bulk result in similar ionization profiles.

profiles on the carrier phase. This might be surprising because for few-cycle pulses the maximal intensity is very sensitive to the carrier phase α_L, see Fig. 13. However, the carrier phase α_L also modulates the number of local intensity maxima; $w_{\sin^2}(\eta,3)$ has for $\alpha_L = 0$ a single pronounced maximum and two side maxima whereas for $\alpha_L = \pi/2$ it has two maxima. Modulation of the number and the height of local intensity maxima in laser pulse by the carrier phase almost cancel each other concerning the ionization probability. The ionization profiles in Fig. 14 have been calculated for rather short pulses with only three half-cycles. For longer pulses, the carrier phase becomes even less important for the ionization probability.

V. ON THE APPLICABILITY OF THE WKB APPROXIMATION

Complementary to our numerical studies of relativistic ionization, one might calculate the ionization probability by analytical semiclassical approximations. Such a theory for electron tunneling in hydrogenlike ions in plane-wave laser fields taking into account relativistic effects was developed by Milosevic *et al.* [49] based on a WKB-like approximation [50,51]. Milosevic *et al.* calculated the ionization rate w, which is related to the ionization probability by $p_{\mathrm{ion}} = 1 - \exp(-wjT)$, where jT denotes the duration of the applied laser field.

While this approach is quite attractive in the tunneling regime, it is based on assumptions that are not fulfilled for

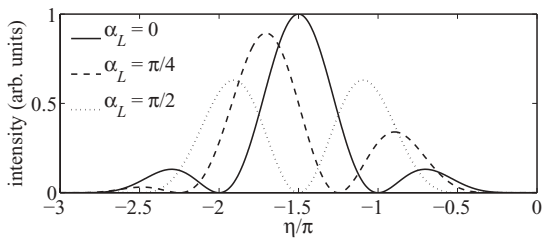

FIG. 13. Laser pulses with the intensity profiles proportional to $[w_{\sin^2}(\eta,3)\sin(\eta + \alpha_L)]^2$ but with different phases α_L. Despite the different phases, all three pulses carry the same energy.

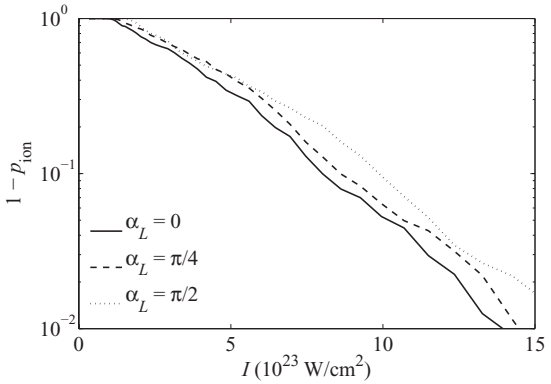

FIG. 14. Occupation probability $1 - p_{\rm ion}$ as a function of the intensity $I = c\varepsilon_0 E_{L,\max}^2/2$ for hydrogenlike ions with $Z = 30$ and laser pulses of wavelength $\lambda = 6.5$ nm and pulse shapes shown in Fig. 13. Ionization profiles are affected marginally by the carrier phase.

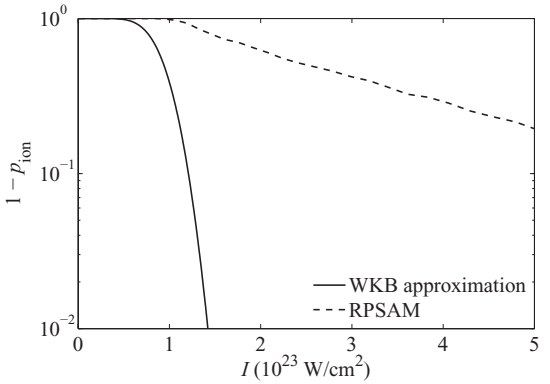

FIG. 15. Occupation probability $1 - p_{\rm ion}$ as a function of the intensity I for $Z = 30$. The solid line shows results predicted by the WKB theory, while the dashed line show $1 - p_{\rm ion}$ as obtained by the application of the relativistic phase-space averaging method (RPSAM).

ionization in ultrahigh-intensity few-cycle laser pulses as considered here. In [49] it is assumed that the ground-state wave function is not significantly changed under the influence of the external laser field. Furthermore, the laser field is modeled by plane waves; effects of the shape of short-time laser pulses are not taken into account. Calculations by Milosevic *et al.* are performed for constant fields and extended to electromagnetic waves by a quasistatic approximation. Therefore, care has to be taken by extrapolating a (semiclassical) tunnel rate into the regime of high field strengths and ultrashort pulses, as it overestimates the ionization probability considerably [52,53]. The WKB approximation gives good results for tunneling through thick and high barriers [54], provided that $\Delta s\sqrt{\bar{V}} > 4$, where Δs is the barrier width in angstroms and $\bar{V}$ is the mean barrier height in electron volts. For tunneling of electrons of hydrogenlike ions in homogeneous electric fields $\boldsymbol{E}$, the condition $\Delta s\sqrt{\bar{V}} > 4$ is violated, e.g., for $|\boldsymbol{E}| > 2.3 \times 10^{13}$ V/m (for $Z = 10$), $|\boldsymbol{E}| > 1.8 \times 10^{14}$ V/m (for $Z = 20$), and $|\boldsymbol{E}| > 6.2 \times 10^{14}$ V/m (for $Z = 30$). If we compare these field strengths to the field strengths in Fig. 2—where we have mostly substantial ionization probabilities beyond the tunneling regime—then we find that the application of the semiclassical tunneling theory of [49] is not justified for ionization in high-intensity laser pulses.

Our numerical calculations support these concerns against the application of the WKB theory in regimes with substantial ionization probabilities. Figure 15 displays the occupation probability $1 - p_{\rm ion}$ as a function of the intensity on a logarithmic scale as obtained from WKB calculations and by the relativistic phase-space averaging method. In both cases, the electron moves in a three-dimensional Coulomb potential. The ionization curves in Fig. 15 deviate significantly. As demonstrated in Sec. IV B the relativistic phase-space averaging method yields an exponential decay of $1 - p_{\rm ion}$ as a function of the laser intensity and plotting the data of Fig. 2 on a semilogarithmic scale the *ab initio* solution of the Dirac equation results the same exponential decay-law, whereas the WKB theory predicts that $1 - p_{\rm ion}$ decreases faster than exponentially. Thus, the WKB theory fails not only quantitatively but also in its qualitative predictions if applied to regimes with substantial ionization probabilities. A generalization of the WKB approach to the over-the-barrier regime, which appears challenging at present, seems attractive.

VI. CONCLUSION

We have investigated the relativistic ionization dynamics of hydrogenlike ions in short intense laser pulses. Perturbative methods, such as the WKB approach, are not suited to model the dynamics in the parameter regime of interest. Thus, we applied two different nonperturbative computational methods, the numerical solution of the time-dependent Dirac equation and the time-dependent Klein-Gordon equation, and the relativistic phase-space averaging method, which we have generalized to arbitrary central potentials in one, two, and three dimensions.

We compared both approaches for one- and two-dimensional systems. For two-dimensional systems classical and quantum mechanical calculations agree better than for one-dimensional systems. For long wavelengths the quantum mechanical ionization probability may be somewhat larger than obtained by the classical relativistic phase-space averaging method due to tunneling. Although the classical relativistic phase-space averaging method does not cover quantum mechanical features, it is often a valuable tool to study ionization in intense laser pulses. For photoionization in intense laser fields classical and quantum mechanical methods give consistent results in the over-the-barrier regime.

The numerical solution of the time-dependent Dirac equation allowed us to study the quantum dynamics of the electron probability density during the ionization process in two dimensions. We also visualized how an increase of the laser field strength affects the motion of the electron's probability density.

In the nonrelativistic limit, the ionization dynamics obeys a scaling relation. The violation of this scaling relation allows to analyze relativistic effects. Relativistic effects tend to lower the ionization threshold intensity but also lower the ionization probability at intensities above the threshold intensity.

Furthermore, we have studied the complex dependence of the ionization probability on the atomic number and on different laser parameters such as the laser wavelength, the

pulse shape, and the carrier phase by means of the relativistic phase-space averaging method. We found that the ionization probability is basically determined by the pulse peak intensity and the number of half-cycles that reach the peak intensity. Therefore, the ionization characteristics of multiply charged hydrogenlike ions may be used to determine the intensity of few-cycle ultrastrong laser pulses with an uncertainty factor of about two.

[1] M. D. Perry and G. Mourou, Science**264**, 917 (1994); M. D. Perry *et al.*, Opt. Lett. **24**, 160 (1999); S.-W. Bahk, P. Rousseau, T. A. Planchon, V. Chvykov, G. Kalintchenko, A. Maksimchuk, G. A. Mourou, and V. Yanovsky, *ibid.* **29**, 2837 (2004); V. Yanovsky *et al.*, Opt. Express **16**, 2109 (2008).

[2] G. Pretzler *et al.*, Phys. Rev. E **58**, 1165 (1998); K. W. D. Ledingham *et al.*, Phys. Rev. Lett. **84**, 899 (2000); T. J. Bürvenich, J. Evers, and C. H. Keitel, *ibid.* **96**, 142501 (2006).

[3] C. H. Keitel, Contemp. Phys. **42**, 353 (2001).

[4] K. W. D. Ledingham, P. McKenna, and R. P. Singhal, Science **300**, 1107 (2003); J. Seres, E. Seres, A. J. Verhoef, G. Tempea, C. Streli, P. Wobrauschek, V. Yakovlev, A. Scrinzi, C. Spielmann, and F. Krausz, Nature (London) **433**, 596 (2005).

[5] G. Brodin, M. Marklund, and L. Stenflo, Phys. Rev. Lett. **87**, 171801 (2001); T. Heinzl, B. Liesfeld, K.-U. Amthor, H. Schwoerer, R. Sauerbrey, and A. Wipf, Opt. Commun. **267**, 318 (2006); A. Di Piazza, K. Z. Hatsagortsyan, and C. H. Keitel, Phys. Rev. Lett. **100**, 010403 (2008).

[6] S. Fritzler, V. Malka, G. Grillon, J. P. Rousseau, F. Burgy, E. Lefebvre, E. d'Humières, P. McKenna, and K. W. D. Ledingham, Appl. Phys. Lett. **83**, 3039 (2003); H. Schwoerer, S. Pfotenhauer, O. Jäckel, K.-U. Amthor, B. Liesfeld, W. Ziegler, R. Sauerbrey, K. W. D. Ledingham, and T. Esirkepov, Nature (London) **439**, 445 (2006); Y. I. Salamin, Z. Harman, and C. H. Keitel, Phys. Rev. Lett. **100**, 155004 (2008).

[7] J. Andruszkow *et al.*, Phys. Rev. Lett. **85**, 3825 (2000).

[8] R. Kienberger *et al.*, Nature (London) **427**, 817 (2004); F. Krausz and M. Ivanov, Rev. Mod. Phys. **81**, 163 (2009).

[9] A. D. Bandrauk, S. Chelkowski, and N. H. Shon, Phys. Rev. Lett. **89**, 283903 (2002).

[10] E. M. Snyder, S. A. Buzza, and A. W. J. Castleman, Phys. Rev. Lett. **77**, 3347 (1996); T. Ditmire, J. W. G. Tisch, E. Springate, M. B. Mason, N. Hay, J. P. Marangos, and M. H. R. Hutchinson, *ibid.* **78**, 2732 (1997); T. Ditmire, E. Springate, J. W. G. Tisch, Y. L. Shao, M. B. Mason, N. Hay, J. P. Marangos, and M. H. R. Hutchinson, Phys. Rev. A **57**, 369 (1998).

[11] P. H. Mokler and T. Stöhlker, in *Advances in Atomic, Molecular, and Optical Physics*, Vol. 37, edited by B. Bederson and H. Walther (Academic Press, 1996), pp. 297–370; J. Ullrich, R. Moshammer, R. Dörner, O. Jagutzki, V. Mergel, H. Schmidt-Böcking, and L. Spielberger, J. Phys. B **30**, 2917 (1997); J. R. C. López-Urrutia *et al.*, J. Phys.: Conf. Ser. **2**, 42 (2004).

[12] H. G. Hetzheim and C. H. Keitel, Phys. Rev. Lett. **102**, 083003 (2009).

[13] E. Gubbini, U. Eichmann, M. Kalashnikov, and W. Sandner, J. Phys. B **38**, L87 (2005); T. Nubbemeyer, K. Gorling, A. Saenz, U. Eichmann, and W. Sandner, Phys. Rev. Lett. **101**, 233001 (2008).

[14] R. Moshammer *et al.*, Phys. Rev. Lett. **98**, 203001 (2007); A. A. Sorokin, S. V. Bobashev, T. Feigl, K. Tiedtke, H. Wabnitz, and M. Richter, *ibid.* **99**, 213002 (2007); S. J. McNaught, J. P. Knauer, and D. D. Meyerhofer, Phys. Rev. A **58**, 1399 (1998).

[15] M. Protopapas, C. H. Keitel, and P. L. Knight, Rep. Prog. Phys. **60**, 389 (1997); T. Brabec and F. Krausz, Rev. Mod. Phys. **72**, 545 (2000); Y. I. Salamin, S. X. Hu, K. Z. Hatsagortsyan, and C. H. Keitel, Phys. Rep. **427**, 41 (2006); G. A. Mourou, T. Tajima, and S. V. Bulanov, Rev. Mod. Phys. **78**, 309 (2006).

[16] S. Geltman, J. Phys. B **33**, 1967 (2000).

[17] The laser field parameter is defined as $\xi = eE_{L,\max}/(mc\omega)$, with the laser field strength $E_{L,\max}$, the frequency ω, the speed of light c, the elementary charge e, and the electron mass m.

[18] S. X. Hu and C. H. Keitel, Phys. Rev. A **63**, 053402 (2001); N. J. Kylstra, R. M. Potvliege, and C. J. Joachain, J. Phys. B **34**, L55 (2001); S. X. Hu, A. F. Starace, W. Becker, W. Sandner, and D. B. Milosevic, *ibid.* **35**, 627 (2002); P. Strange, *Relativistic Quantum Mechanics* (Cambridge University Press, 1998).

[19] G. R. Mocken and C. H. Keitel, J. Comput. Phys. **199**, 558 (2004); Comput. Phys. Commun. **178**, 868 (2008).

[20] M. Ruf, H. Bauke, and C. H. Keitel, J. Comput. Phys. **228**, 9092 (2009).

[21] R. Abrines and I. C. Percival, Proc. Phys. Soc. **88**, 861 (1966); **88**, 873 (1966); I. C. Percival, Comput. Phys. Commun. **6**, 347 (1973); J. G. Leopold and I. C. Percival, J. Phys. B **12**, 709 (1979).

[22] H. Schmitz, K. Boucke, and H.-J. Kull, Phys. Rev. A **57**, 467 (1998).

[23] H. Feshbach and F. Villars, Rev. Mod. Phys. **30**, 24 (1958).

[24] M. D. Feit, J. A. Fleck Jr., and A. Steiger, J. Comput. Phys. **47**, 412 (1982).

[25] J. W. Braun, Q. Su, and R. Grobe, Phys. Rev. A **59**, 604 (1999).

[26] U. W. Rathe, C. H. Keitel, M. Protopapas, and P. L. Knight, J. Phys. B **30**, L531 (1997); U. W. Rathe, P. Sanders, and P. L. Knight, Parallel Computing **25**, 525 (1999).

[27] C. H. Keitel and P. L. Knight, Phys. Rev. A **51**, 1420 (1995); L. N. Gaier and C. H. Keitel, *ibid.* **65**, 023406 (2002).

[28] J. S. Cohen, Phys. Rev. A **26**, 3008 (1982).

[29] T. H. Boyer, Am. J. Phys. **72**, 992 (2004).

[30] The point of closest approach is called the pericenter.

[31] W. Krauth, *Statistical Mechanics: Algorithms and Computations* (Oxford University Press, 2006); D. P. Landau and K. Binder, *A Guide to Monte Carlo Simulations in Statistical Physics*, 3rd ed. (Cambridge University Press, 2009).

[32] H. W. Schranz, S. Nordholm, and G. Nyman, J. Chem. Phys. **94**, 1487 (1990).

[33] K. G. Kay, J. Chem. Phys. **100**, 4377 (1994); G. van de Sand and J. M. Rost, Phys. Rev. Lett. **83**, 524 (1999); Phys. Rev. A **62**, 053403 (2000).

[34] J. G. Leopold and I. C. Percival, Phys. Rev. Lett. **41**, 944 (1978).

[35] G. Duchateau, E. Cormier, and R. Gayet, The European Physical Journal D—Atomic, Molecular, Optical and Plasma Physics **11**, 191 (2000).

[36] J. Grochmalicki, M. Lewenstein, and K. Rzążewski, Phys. Rev. Lett. **66**, 1038 (1991).

[37] S. X. Hu and A. F. Starace, Phys. Rev. E **73**, 066502 (2006).
[38] N. T. Maitra and E. J. Heller, Phys. Rev. A **54**, 4763 (1996); Phys. Rev. Lett. **78**, 3035 (1997); R. Côté, H. Friedrich, and J. Trost, Phys. Rev. A **56**, 1781 (1997).
[39] P. J. Mohr, G. Plunien, and G. Soff, Phys. Rep. **293**, 227 (1998); V. M. Shabaev, V. A. Yerokhin, T. Beier, and J. Eichler, Phys. Rev. A **61**, 052112 (2000).
[40] G. R. Mocken and C. H. Keitel, Phys. Rev. Lett. **91**, 173202 (2003).
[41] Note the misspelling of the x axis of Fig. 2 of the original work (Ref. [12]). Instead of ionic charge it should be nuclear charge Z.
[42] For convenience, one may set $\alpha' = 1$.
[43] J. Görlinger, L. Plagne, and H.-J. Kull, Appl. Phys. B **71**, 331 (2000).
[44] G. M. Fraiman, V. A. Mironov, and A. A. Balakin, Phys. Rev. Lett. **82**, 319 (1999).
[45] J. R. Schneider, R. H. Nielsen, J. Feldhaus, B. Keitel, W. L. P. Schmüser, B. Sonntag, and K. Tiedtke, FLASH: The Free-Electron Laser in Hamburg, Tech. Rep. Deutsches Elektronen-Synchrotron DESY, 2007.
[46] M. Altarelli *et al.*, The European X-Ray Free-Electron Laser Technical design report, Tech. Rep., DESY XFEL Project Group, European XFEL Project Team, Deutsches Elektronen-Synchrotron, 2007.
[47] M. Klaiber, K. Z. Hatsagortsyan, and C. H. Keitel, Phys. Rev. A **74**, 051803(R) (2006).
[48] A. Baltuška *et al.*, Nature (London) **421**, 611 (2003).
[49] N. Milosevic, V. P. Krainov, and T. Brabec, Phys. Rev. Lett. **89**, 193001 (2002); J. Phys. B **35**, 3515 (2002).
[50] M. Razavy, *Quantum Theory of Tunneling* (World Scientific, Singapore, 2003).
[51] D. F. Ye, G. G. Xin, J. Liu, and X. T. He, J. Phys. B **43**, 235601 (2010).
[52] N. B. Delone and V. P. Krainov, Phys. Usp. **41**, 469 (1998).
[53] A. Scrinzi, M. Geissler, and T. Brabec, Phys. Rev. Lett. **83**, 706 (1999).
[54] K. H. Gundlach and J. G. Simmons, Thin Solid Films **4**, 61 (1969).